

Additive Engineering Enables Ionic-Liquid Electrolyte-Based Supercapacitors To Deliver Simultaneously High Energy and Power Density

Xinglin Jiang, Xinzhen Wu, Yanting Xie, Zixing Wang, Junfeng Huang, Yuanxiao Qu, Dali Mu, Xiong Zhang, Weiqing Yang, and Haitao Zhang*



Cite This: *ACS Sustainable Chem. Eng.* 2023, 11, 5685–5695



Read Online

ACCESS |

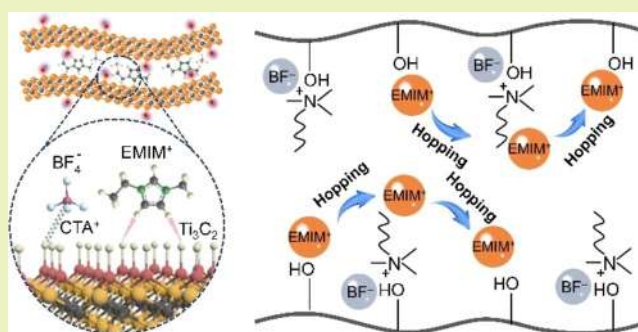
Metrics & More

Article Recommendations

Supporting Information

ABSTRACT: Ionic liquid (IL) electrolytes with a high potential window are promising candidates to high-energy-density supercapacitors; however, they commonly suffer from serious kinetic barriers that lead to poor power density. In this work, we propose an additive engineering method to promote rapid dynamics of IL-based supercapacitors. Additive engineering is based on adding cetyltrimethylammonium bromide-grafted Ti_3C_2 MXene (Ti_3C_2 -CTAB) into 1-ethyl-3-methylimidazolium tetrafluoroborate (EMIMBF_4), a typical IL electrolyte for supercapacitors. Remarkably, IL electrolytes show a considerable increase by 38% in ionic conductivity and great reduction in solid–liquid surface energy from 18.03 to 12.37 mN m^{-1} . We prove that electrostatic force and hydrogen bonds generated from the interaction between Ti_3C_2 -CTAB and EMIMBF_4 facilitate considerable dissociation of electrolyte ion pairs and ion-transfer capability. Consequently, additive engineering-designed IL-based supercapacitors deliver simultaneously a high energy density of 28.3 Wh kg^{-1} and power density of 18.3 kW kg^{-1} . The increased high-power characteristics are supported by a faster ion diffusion coefficient (1.50×10^{-12} vs $4.04 \times 10^{-13} \text{ cm}^2 \text{ s}^{-1}$) and shorter relaxation time (3.83 vs 6.81 s). In addition, additive engineering guarantees a stable cycling life of 83.6% capacitance retention after 9000 cycles at the depth potential window from 0 to 3.0 V.

KEYWORDS: additive engineering, supercapacitors, ionic liquid, MXene, power density, energy density



INTRODUCTION

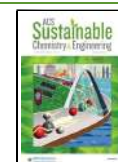
Supercapacitors have recently attracted great attention due to their high-power density, fast charging/discharging capability, and long cycle life.^{1–10} However, the maximal shortcoming of supercapacitors is their low energy density, only about 1/10 ~ 1/15 of Li-ion batteries.^{11–16} As an indispensable component in supercapacitors, electrolytes and their synchronization with electrodes are responsible for high energy density as well as rapid dynamics and long-term stability.^{17,18} Generally, the ionic conductivity, permittivity, and stability including thermodynamic, dynamic, and electrochemical stability are the key parameters to develop better electrolytes to promise high energy density, rapid charging, and high sustainable supercapacitors.^{19,20} Taking into consideration of excellent ionic conductivity of aqueous electrolytes, the first RuO_2 -based supercapacitors used in the military field adopted H_2SO_4 aqueous solution electrolyte to realize their large-current and high-power characteristics.²¹ However, due to the limitation of water decomposition potential (commonly <1.23 V), aqueous solution electrolytes exhibited pretty low energy density ($\sim 2.0 \text{ Wh kg}^{-1}$) in supercapacitors.²² In comparison, organic

electrolytes with a much high electrochemically stable potential (2.5–3.0 V) considerably increase the energy density ($\sim 7.0 \text{ Wh kg}^{-1}$) of active carbon-based supercapacitors that dominate the present commercial market. Remarkably, MAXWELL broadened the potential window of organic-based supercapacitors from 2.7 to 2.85 V and further to 3.0 V, which efficiently increased the energy density by $\sim 20\%$. Actually, to maximize energy density, the electrolytes in advanced supercapacitors are often pushed to operate at extreme potentials, where thermodynamical and electrochemical stabilities become particularly significant.²³ In this regard, ionic liquid (IL) electrolytes with an extremely high operating potential window (up to 5.0 V) become a promising

Received: January 12, 2023

Revised: March 21, 2023

Published: March 30, 2023



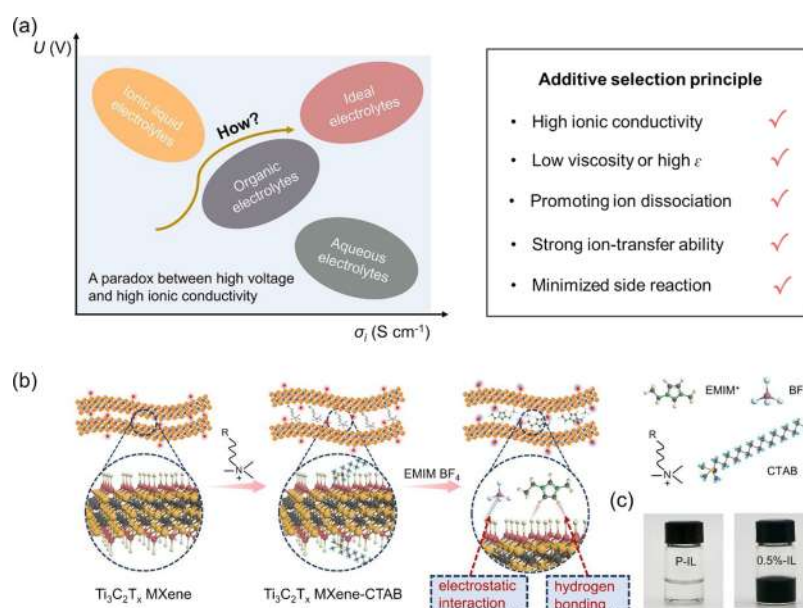


Figure 1. Designing better IL electrolytes by additive engineering. (a) Plot of conductivity (σ_i) versus operating potential window (U) for different electrolytes and additive selection principle; (b) schematic illustration of designing Ti_3C_2 -CTAB decorated EMIMBF₄ electrolyte, in which hydrogen bonding and electrostatic interaction are critical to promote the dissociation of EMIMBF₄; (c) optical images of EMIMBF₄ electrolytes with (right panel) and without (left panel) Ti_3C_2 -CTAB additives (0.5 wt %).

candidate for developing high-energy-density supercapacitors.²⁴

IL salts commonly composed of organic cations and organic/inorganic anions are liquid at room temperature. The physicochemical and electrochemical properties of the IL can also be tuned via multiple coupling of cations and anions.²⁵ Although a much higher energy density (up to $\sim 120 \text{ Wh kg}^{-1}$ based on mere electrode materials) has been realized in supercapacitors, IL-based supercapacitors still hold the main disadvantage of low power density.²⁶ This low power characteristic is originated from the sluggish ion transfer kinetics mainly induced by strong cation–anion attraction in neat IL electrolyte.^{27,28} To overcome this, some strategies have been reported to improve ionic conductivity and hence promoted power performance of IL-based supercapacitors. The first method is the construction of eutectic IL electrolytes. For example, *N*-butyl-*N*-methylpyrrolidinium bis (fluorosulfonyl) imide (PYR₁₄-FSI) and *N*-methyl-*N*-propylpiperidinium bis (fluorosulfonyl) imide (PIP₁₃-FSI) eutectic mixtures shared a dense ionic arrangement through weakening the inherent cation–anion attraction in ILs.²⁹ The second method is the introduction of organic liquids into IL electrolytes, which realizes high ionic conductivity by reducing the viscosity of IL electrolytes.^{30,31} The third method is the addition of redox-active media to the IL, and the effect lies in the decline of charge transfer resistance.^{32,33} However, these proposed strategies still exhibit two apparent issues: one is lowering the electrochemical stability window that is paradox to high energy and power supercapacitors; another is severely deteriorating the energy density during long-term cycling processes.³⁴ We can conclude that overcoming low ionic conductivity of IL electrolytes without compromising the potential window and stability is fundamentally challenging yet technically critical for developing simultaneously high energy and power IL-based supercapacitors.

In this work, we propose a method of additive engineering to high ionic conductive IL electrolytes without sacrificing the

operation potential window and electrochemical stability. In principle, the ideal additive needs to meet the demand of high ionic conductivity, low viscosity or high dielectric constant, promoted ion dissociation, strong ion-transfer ability, and minimized side reaction (Figure 1a). Herein, the proposed additive engineering is on the basis of introducing cetyltrimethylammonium bromide (CTAB)-grafted Ti_3C_2 into 1-ethyl-3-methylimidazolium tetrafluoroborate (EMIMBF₄) (Figure 1b). With the decoration of CTAB, Ti_3C_2 can be stably dispersed in EMIMBF₄ with the help of sonication (Figure 1c). After short-time and mild sonication, the Ti_3C_2 MXenes retain their large nanosheets and hence guarantee high conductivity. More importantly, the anionic groups (–O and –OH groups) and cationic groups (–NH₄⁺) simultaneously exist on Ti_3C_2 -CTAB, which form hydrogen bonding and electrostatic interaction with EMIM⁺ and BF₄[–], respectively (see Figure 1b). These two positive effects supply the dual-active binding sites to promote the dissociation of EMIM⁺ and BF₄[–] in EMIMBF₄ IL electrolyte, leading to fast migration of ions during charging/discharging and thus enhancing power characteristics of supercapacitors.

RESULTS AND DISCUSSION

The interlayer spacings of Ti_3C_2 and Ti_3C_2 -CTAB were characterized by X-ray diffraction (XRD). As shown in Figure S1a, after the insertion of CTAB, the (002) peak of the Ti_3C_2 powder shifts significantly from a 2θ angle of 6.44° ($d = 1.371 \text{ nm}$) to a 2θ angle of 5.82° ($d = 1.517 \text{ nm}$), which indicates that CTAB was grafted on the surface of Ti_3C_2 successfully. Figure S1b shows the thermogravimetric analysis (TGA) curves of CTAB, Ti_3C_2 , and Ti_3C_2 -CTAB. It displays that Ti_3C_2 has a slight thermal weight loss at $200\text{--}400^\circ\text{C}$, which is caused by the thermal degradation of the terminating groups (–O, –OH, –F, and –Cl).³⁵ In addition, the thermal stability of Ti_3C_2 -CTAB is worse compared to that of Ti_3C_2 because the decorated CTAB will lose weight in the temperature range of $200\text{--}300^\circ\text{C}$. It can be seen that the weight losses of Ti_3C_2

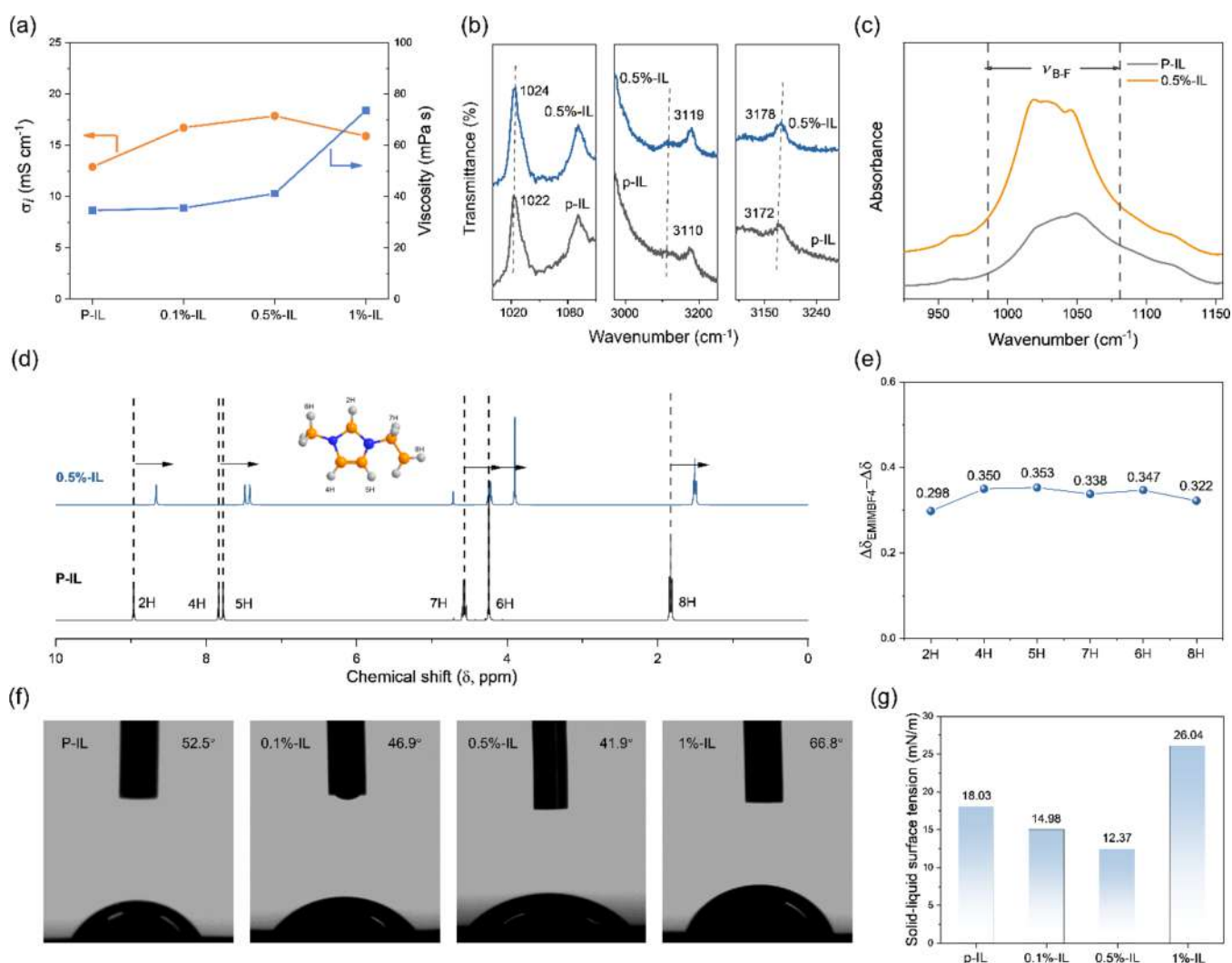


Figure 2. Improved properties of EMIMBF₄ IL electrolyte by additive engineering. (a) Ionic conductivity and viscosity of different electrolytes. (b) Raman spectra, (c) ATR-IR spectra, and (d) ¹H NMR spectra of P-IL and 0.5%-IL. (e) Chemical shift of different H sites. (f) Contact angle and (g) according solid-liquid surface tension of different electrolytes on the activated carbon electrode.

and Ti₃C₂-CTAB are 2.24 and 33.01 wt %, respectively, when the temperature is 700 °C. This result demonstrates that 30.77 wt % of CTAB has been successfully grafted onto the surface of Ti₃C₂.

We first proved that the additive engineering could increase room-temperature ionic conductivity of IL electrolytes. The average ionic conductivity of neat EMIMBF₄ (P-IL) is 12.91 mS cm⁻¹ as shown in Figure 2a and Table S1. The decorated EMIMBF₄ electrolytes were named according to the relative mass ratio of Ti₃C₂-CTAB to IL, such as 0.1%-IL, 0.5%-IL, and 1%-IL, respectively. As the mass fraction of the Ti₃C₂-CTAB additive increased from 0.1 to 0.5 wt %, the ionic conductivity of the electrolyte gradually increased, and a threshold was observed in 0.5%-IL with a maximum value of 17.87 ± 0.12 mS cm⁻¹, a considerable 38% increase compared to that of P-IL. Then, the ionic conductivity gradually decreased with the further increase in the mass ratio of Ti₃C₂-CTAB. This variation in ionic conductivity through additive engineering could be explained as following. In the absence of Ti₃C₂-CTAB, the strong interaction between anions and cations in EMIMBF₄ as called co-ion pairs leads to low ion mobility that is the reason for low ionic conductivity.³⁶ An apparent

increment in ionic conductivity with an optimal Ti₃C₂-CTAB additive is observed as the introduction of Ti₃C₂-CTAB provides a migration channel for EMIMBF₄, which greatly increases the migration rate of anions and cations. The increased ionic conductivity was also observed in 1-butyl-3-methylimidazolium tetrafluoroborate (BMIMBF₄), Ti₃C₂-CTAB was mixed with BMIMBF₄ at a mass ratio of 0.5:100, and the obtained ionic liquid was denoted as BMIMBF₄@Ti₃C₂-CTAB. The average ionic conductivity of neat BMIMBF₄ is 2.92 mS cm⁻¹ as shown in Table S2. With the addition of Ti₃C₂-CTAB, the ionic conductivity of the electrolyte increases to 4.21 mS cm⁻¹, a considerable 44% increase compared to that of neat BMIMBF₄. However, the excess of Ti₃C₂-CTAB prevents ion transport vice versa because of the stack of Ti₃C₂ nanosheets, leading to the declined ionic conductivity. For comparison, we also prepared EMIMBF₄ electrolytes containing 0.5 wt % of Ti₃C₂ or CTAB, which were labeled as Ti₃C₂-IL and CTAB-IL, respectively. The conductivity decreased to 12.75 and 12.01 mS cm⁻¹ as Ti₃C₂ or CTAB was added to the ionic liquid alone, respectively (Table S1). The slight decrease in the conductivity of Ti₃C₂-IL can be explained by the undesirable solubility of

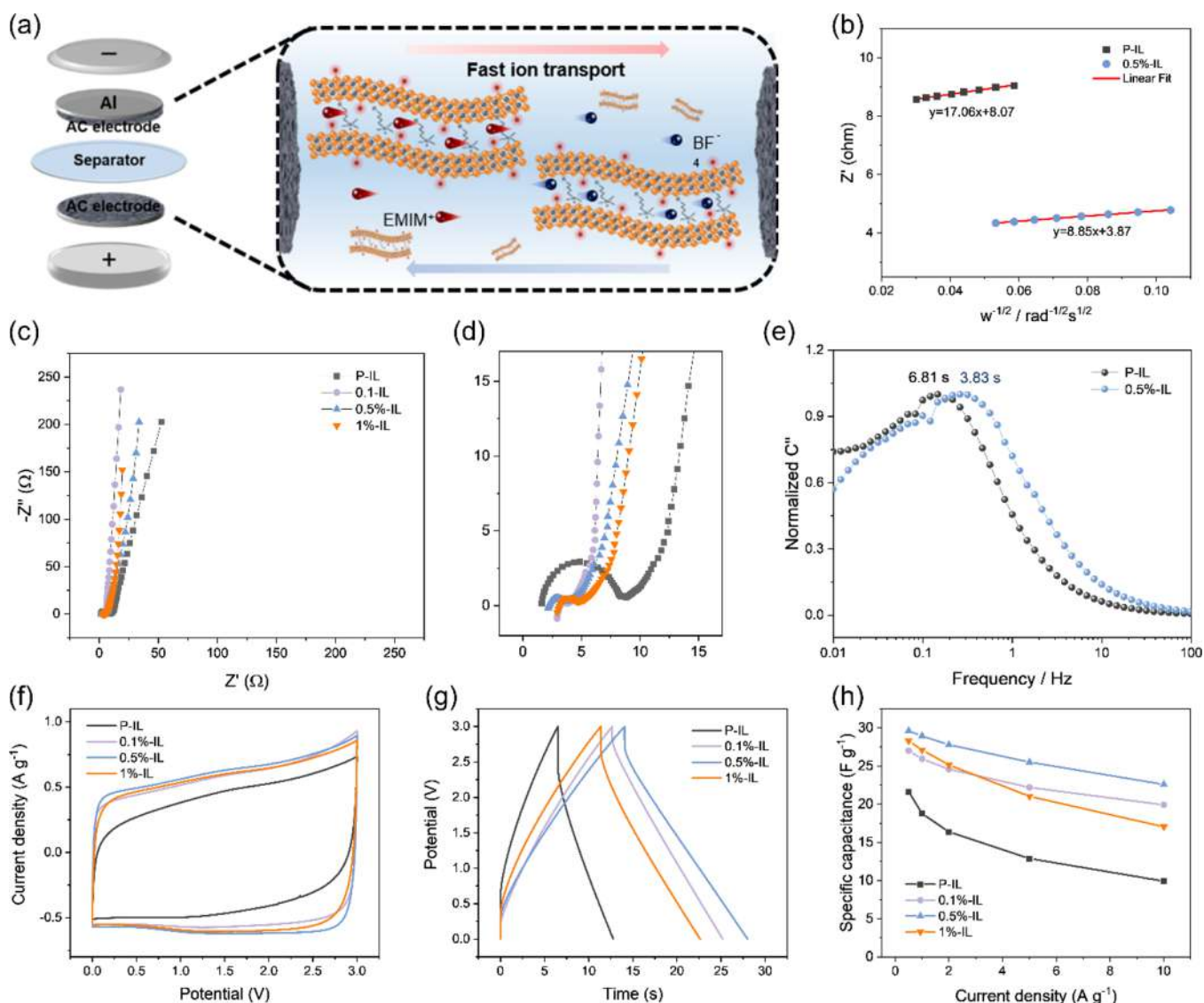


Figure 3. The electrochemical performance of P-IL and different concentration additive supercapacitors. (a) Schematic illustration of the diffusion process in the additive engineering electrolytes; (b) relationship between Z' and $\omega^{-1/2}$ in the low-frequency part calculated from EIS measurement results; (c) Nyquist plots for the P-IL, 0.1%-IL, 0.5%-IL, and 1%-IL; (d) Nyquist plots for the high-frequency region; (e) the normalized imaginary part capacitance (C''); (f) CV curves at a scan rate of 20 mV s⁻¹; (g) GCD curves at a current density of 5 A g⁻¹; (h) the mass specific capacitance of P-IL, 0.1%-IL, 0.5%-IL, and 1%-IL supercapacitors by GCD curves.

Ti₃C₂ in EMIMBF₄ (as shown in the optical image of Figure S2), and the Ti₃C₂ layer stacked in the ionic liquid results in a much higher viscosity of electrolyte. However, the decrease in the conductivity of CTAB-IL is mainly caused by the low conductivity of CTAB itself. The viscosity of EMIMBF₄ IL electrolytes was also changed after experiencing additive engineering. As the Ti₃C₂-CTAB concentration increases from 0.1 to 0.5 wt %, the value of viscosity increases slightly. As Ti₃C₂-CTAB is further increased, the viscosity increases sharply in 1%-IL, causing the decline of ionic conductivity.

In order to reveal the underlying reason of additive engineering leading to the increased ionic conductivity of EMIMBF₄ IL electrolytes, spectral analyses of the electrolytes were carried out. Raman spectroscopy was used to explore the evolution of the hydrogen bonds (H-bonds) in the Ti₃C₂-CTAB and EMIMBF₄ complexes. The full Raman spectra ranging from 400 to 4000 cm⁻¹ are shown in Figure S3. Some characteristic Raman peaks are shown in Figure 2b. The peaks

at 1022 cm⁻¹ represent the bending vibration of C-4(5)H (the inset of Figure 2b), and the peaks near 3110 and 3172 cm⁻¹ are ascribed to the C-2H (the inset of Figure 2b) and C-4(5)H stretching vibrations on the imidazole ring of the EMIM⁺ cations.^{37,38} As for the 0.5%-IL sample, the bending vibration of C-4(5)H and the stretching vibrations of C-2H and C-4(5)H exhibit a clear red shift to 1024, 3119, and 3178 cm⁻¹, respectively. This variation tendency indicated the strong interplay between the active H sites and Ti₃C₂-CTAB, which destroyed the original electrostatic balance between the anion and cation groups in EMIMBF₄ and generated hydrogen bonds between EMIM⁺ and Ti₃C₂-OH via ion-dipole interactions (⁺C-H...OH-Ti).³⁹ For Ti₃C₂-IL and CTAB-IL, these characteristic peaks were noticeable shifted, which implies that the original electrostatic balance between the anionic and cationic groups in EMIMBF₄ was not destroyed (Figure S4). On the other hand, the generation of electrostatic interaction between CTAB and EMIMBF₄ was proved by

attenuated total reflection infrared spectroscopy (ATR-IR) characterization (Figure S5). As shown in Figure 2c, the ATR-IR spectra of P-IL and 0.5%-IL illustrate B–F stretching mode with the band ranging from 975 to 1075 cm^{-1} . Apparently, 0.5%-IL showed a broad band and it could be deconvoluted into three peaks, an indicator of electrostatic interaction between BF_4^- and $\text{Ti}_3\text{C}_2\text{A}^+$.⁴⁰ In short, Raman and ATR-IR spectra disclosed that the improved ionic conductivity of EMIMBF₄ by additive engineering was attributed from the generated additional hydrogen bonds and electrostatic interaction between the additives and IL electrolytes.

¹H nuclear magnetic resonance spectroscopy (NMR) was further utilized to detect the chemical states of the H-bonds in neat EMIMBF₄ and their evolution after adding $\text{Ti}_3\text{C}_2\text{-CTAB}$.⁴¹ As shown in Figure 2d, the chemical shift (δ) values in the descending order of EMIMBF₄ were 2H (8.963 ppm), 4H (7.834 ppm), 5H (7.773 ppm), 7H (4.571 ppm), 6H (4.244 ppm), and 8H (1.827 ppm). The incorporation of $\text{Ti}_3\text{C}_2\text{-CTAB}$ resulted in the red shift of active hydrogen in the rings of EMIMBF₄ (Table S3). Noteworthy, the chemical shifts of 4H and 5H were decreased by 0.350 and 0.353 ppm, respectively, which were much larger than the change of other H sites, indicating the intense interaction between $\text{Ti}_3\text{C}_2\text{-CTAB}$ and 4(S)H. The intense interaction of $\text{Ti}_3\text{C}_2\text{-CTAB}$ with 4H and 5H was attributed to the fact that the electron-withdrawing effect triggered by the H-bonding interaction with the F[−] atom in the BF_4^- anion ($^+\text{C}-\text{H}\cdots\text{F}-\text{B}^-$), by which 4H and 5H possess more positive charges than 2H, 6H, 7H, and 8H, located outside the imidazole ring. Therefore, with the addition of $\text{Ti}_3\text{C}_2\text{-CTAB}$ to EMIMBF₄, 4(S)H interacts more intensely with the large electronegative –OH group on the surface of Ti_3C_2 .⁴² In fact, the chemical shifts of H peaks after adding $\text{Ti}_3\text{C}_2\text{-CTAB}$ were much larger than that of previously reported work,^{42,43} demonstrating that $\text{Ti}_3\text{C}_2\text{-CTAB}$ was an excellent dissociator to break up the ion pairs of EMIMBF₄.

To investigate the thermal stability of additive engineering electrolyte, the TGA analyses were performed on P-IL and 0.5%-IL. As shown in Figure S6, the derivative thermogravimetry (DTG) curves of P-IL and 0.5%-IL showed only a single endothermic peak, appearing at 441 and 438 °C, respectively, which could be attributed to decomposition of the ionic liquid. The 0.5%-IL electrolyte was stable up to 384 °C, which is similar to 388 °C of the P-IL; the similarly high onset decomposition temperature means that additive-engineered electrolyte is fully capable of meeting the thermal stability requirements of supercapacitors.

Direct wetting behaviors of P-IL, 0.1%-IL, 0.5%-IL, and 1%-IL on activated carbon electrodes were also measured. As shown in Figure 2f, the average initial contact angle P-IL is 52.5° while it sharply declines to 41.9° for 0.5%-IL, indicating rapid ion-sorption dynamics in 0.5%-IL. Moreover, we determined the solid–liquid surface tension (γ_{sl}) according to the ZDY method as following.⁴⁴

$$\gamma_{\text{sl}} = \frac{\gamma_1}{2} (\sqrt{1 + (\sin\theta)^2} - \cos\theta) \quad (1)$$

where γ_1 is the surface tension, and θ is the contact angle between the solid and the liquid. As shown in Figure 2g, EMIMBF₄ has a surface tension of 0.054 N/m and an according solid–liquid surface tension of 18.03 mN/m at 25 °C. In contrast, the solid–liquid surface tension decreases as $\text{Ti}_3\text{C}_2\text{-CTAB}$ increases, reaching a threshold value of 12.37 mN/m in 0.5%-IL, demonstrating the improved wettability of

the $\text{Ti}_3\text{C}_2\text{-CTAB}$ and EMIMBF₄ complexes to the activated carbon electrodes. Again, the increased solid–liquid surface tension in 1%-IL was due to the aggregation of Ti_3C_2 nanosheets and high viscosity.

After unraveling the increased ionic conductivity, the promoted ion dissociation, and the improved wettability of EMIMBF₄ electrolyte through additive engineering, we demonstrated that the ion-transfer dynamics were also accelerated, which guaranteed high-power performance of supercapacitors. First, coin-typed supercapacitors (CR2032) were assembled using IL electrolytes and activated carbon (YPS0F) as the electrodes to evaluate the electrochemical performance (Figure 3a). As shown in Figure 3b, the diffusion coefficients for P-IL and 0.5%-IL were calculated to be 4.04×10^{-13} and $1.50 \times 10^{-12} \text{ cm}^2 \text{ s}^{-1}$, respectively.^{45,46} The higher value occurred for 0.5%-IL implied that the diffusion dynamics of ions in 0.5%-IL electrolytes over AC electrodes could be established more rapidly. Figure 3c shows the Nyquist plots with a frequency range of 10 mHz to 10 kHz. R_{ct} refers to the charge transfer resistance at the electrolyte/electrode interface. The results showed that the P-IL assembled supercapacitors had a high R_{ct} of 6.2 Ω , while all the $\text{Ti}_3\text{C}_2\text{-CTAB}$ and EMIMBF₄ complexes exhibited largely declined R_{ct} values that are 0.4, 1.3, and 1.4 Ω in 0.1%-IL, 0.5%-IL, and 1%-IL, respectively. In addition, a characteristic relaxation time constant τ_0 can be calculated from the reciprocal of the characteristic frequency f corresponding to the maximum C'' .⁴⁷ It is noted that the τ_0 value for 0.5%-IL is 3.83 s, which is much lower than that of P-IL (6.81 s, Figure 3e), further indicating the superior ion diffusion rate of additive engineering designed electrolytes.

The electrochemical stability window was obtained from the linear sweep voltammetry (LSV) for the P-IL and 0.5%-IL electrolytes as shown in Figure S7. From the voltammogram, it is observed that the overall electrochemical potential windows for the P-IL and 0.5%-IL electrolytes are almost identical (4.2 V), where the cathodic and anodic potentials are −1.8 and 2.4 V versus Ag/AgCl, respectively. This result indicates that additive engineering does not sacrifice the electrochemical window of the EMIMBF₄ electrolyte. The cyclic voltammetry (CV) curves were obtained in the voltage range of 0–3 V as shown in Figure S8. All the CV curves showed a favorable quasi-rectangular shape at a scan rate of 20 mV s^{-1} (Figure 3f), corresponding to their ideal electric double layer energy storage behavior. Integrated CV curves indicated that the additive engineered-based supercapacitors possessed a higher specific capacitance than the P-IL supercapacitors because of their larger area. Among them, the 0.5%-IL supercapacitors were the largest, corresponding to the highest specific capacitance. As shown in Figure 3g, the galvanostatic charging–discharging (GCD) curves of 0.5%-IL supercapacitors also displayed a regular inverted triangle shape and had a small voltage drop (0.3 V) at 5 A g^{-1} , which is lower than that of the P-IL (up to 1.1 V) supercapacitors, demonstrating the low charge transfer resistance of 0.5%-IL supercapacitors. The mass specific capacitances at different current densities were calculated according to the GCD curve (Figure S9). As expected, the 0.5%-IL supercapacitors delivered the highest capacitance value up to 29.6 F g^{-1} , superior to those of P-IL supercapacitors (21.6 F g^{-1} , Figure 3h). Noted that the 0.5%-IL supercapacitors can still retain 22.6 F g^{-1} at 10 A g^{-1} , corresponding to a 76.4% capacitance retention. In contrast, P-

IL supercapacitors only shared a 45.8% retention from 0.5 to 10 A g⁻¹.

We further explored the high-temperature and low-temperature performance of additive engineering based-supercapacitors. Figure S10a and 10d shows Nyquist plots of P-IL and 0.5%-IL supercapacitors at -10 and 50 °C, respectively. The 0.5%-IL supercapacitor exhibited a straight line with a larger slope in the low frequency region at both low temperatures and high temperatures, indicating that the addition of Ti₃C₂ to the ionic liquid facilitates the reduction of the ion diffusion resistance at both high and low temperatures. In addition, at -10 °C, the charge transfer resistance (R_{ct}) of the 0.5%-IL supercapacitor inferred from the semi-circles is 4.1 Ω, which is lower than 6.4 Ω of the P-IL supercapacitor. Similarly, when the testing temperature increases to 50 °C, the R_{ct} of 1.7 Ω for the 0.5%-IL supercapacitor is lower than 3.1 Ω for the P-IL supercapacitor. These results proved that 0.5%-IL exhibited a better ion diffusion behavior than P-IL at both low and high temperatures. GCD tests were also conducted to evaluate the capacitive behavior of supercapacitors based on P-IL and 0.5%-IL at -10 and 50 °C, respectively (Figure S10b and 10e). It was found that a smaller voltage drop was achieved by 0.5%-IL than by P-IL at both low and high temperatures. Figure S10c and 10f shows plots of the specific capacitance as a function of current density for the P-IL and 0.5%-IL supercapacitors measured at -10 and 50 °C, respectively. At -10 °C, a capacitance of 15.7 F g⁻¹ was attained when the 0.5%-IL supercapacitor was used at 0.5 A g⁻¹, exceeding 11.2 F g⁻¹ for the P-IL supercapacitor. When operated at a large current density of 10 A g⁻¹, the 0.5%-IL supercapacitor still retained a greater capacitance retention than the P-IL supercapacitor (18.5% vs 4.5%). Similarly, at a high temperature of 50 °C, 0.5%-IL supercapacitors showed a higher specific capacitance (30.3 F g⁻¹ vs 28.5 F g⁻¹) and higher rate capability (75.9% vs 73.3%) than P-IL supercapacitors.

The Ragone plot is shown in Figure 4. Clearly, 0.5%-IL-based supercapacitors reveal a considerable energy density of

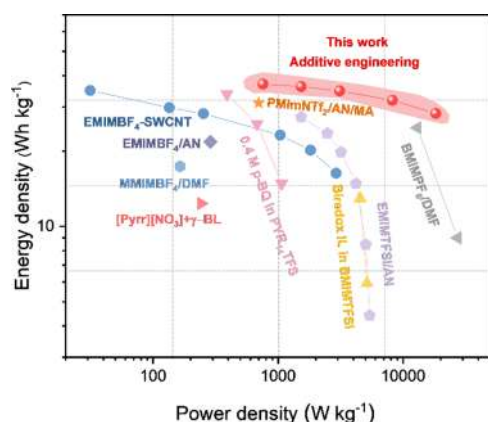


Figure 4. Ragone plots of additive engineering-based supercapacitors in comparison with previously reported studies.

37 Wh kg⁻¹ at a power density of 756 W kg⁻¹. Even at a high power density of 18.3 kW kg⁻¹, the device can simultaneously deliver a high energy density of 28.3 Wh kg⁻¹, indicating excellent rate performance. As a result, this work outperforms many previously reported studies regarding electrolyte modification-based supercapacitors in terms of both energy density and power density (Table S4).^{32,33,48–54}

To further demonstrate the universality of the proposed additive engineering, we also assembled supercapacitors with activated carbon electrodes and tetraethylammonium tetrafluoroborate/propylene carbonate (Et₄NBF₄/PC) commercial electrolyte. As shown in Figure S11, the Nyquist plots demonstrate that the R_{ct} value was 6.3 Ω with the neat Et₄NBF₄/PC as the electrolyte, while it was largely reduced to 1.8 Ω with the addition of 0.5 wt % Ti₃C₂-CTAB in Et₄NBF₄/PC. Therefore, the proposed additive engineering strategy is also applicable for promoting fast ion transport in commercial electrolyte-based supercapacitors.

The additive engineering did enhance the energy density and high rate capability of IL-based supercapacitors. We would prove that the electrochemical stability was also improved. The cycling stability of IL-based supercapacitors was tested at a current density of 5 A g⁻¹. As shown in Figure 5a, after 9000 cycles, the charge/discharge times of P-IL supercapacitors are shortened and the voltage drop is increased, yielding a very low capacitance retention value of 59.8%. In contrast, the GCD curve of 0.5%-IL supercapacitors could still maintain their triangle shape with very little reduction on the voltage drop, resulting in a relatively high capacitance retention value of 83.6%. The outstanding cycling stability of the additive engineering supercapacitor is comparable or even exceeds that of some previously reported work on supercapacitors based on the increased ionic conductivity of ionic liquids (Table S5).^{31,55–60} Figure 5b shows the Nyquist plots of these devices before and after cycling. The R_{ct} values increase to a large extent for the P-IL supercapacitors after cycling, however, the incline tendency of the semicircle is also present while greatly suppressed for the 0.5%-IL supercapacitors.

Next, we analyzed the structural and morphological variation after the cycling test. Raman spectroscopy was used to detect the change in the electrode's microstructure. To avoid any interference of the electrolytes during the physicochemical characterizations, EMIMBF₄ was removed from the aged electrodes by several successive washes with deionized water prior to the post-mortem analyses. The Raman spectra demonstrated the disordered structure of the materials with two peaks at 1350 and 1580 cm⁻¹ that were assigned to the D-band (the defects or disordered in samples) and G-band (the graphitic order) (Figure 5c).⁶¹ The value of I_D/I_G indicates the disordered or defected degree of the carbon materials. As shown in Figure 5d, compared with the pristine one with I_D/I_G = 1.16, the AC electrodes displayed a higher value I_D/I_G of 1.51 after cycling in P-IL electrolyte, implying that higher structural defects emerged in electrodes. However, after the same cycling, the AC electrode in the 0.5%-IL electrolyte showed an I_D/I_G value of 1.19, similar to the pristine AC electrode. This result demonstrated that the additive engineering prevented the interfacial resistance between electrode/electrolyte, which was probably responsible for stable long-term cycling.

Further, we demonstrated monolithic pouched supercapacitors with 4.1 F at 0.5 mA cm⁻² (single-layer with an area of 70 × 40 mm for positive and negative electrode) and laminated pouched supercapacitors with 48.8 F at 3 mA cm⁻² (30-layers with an area of 50 × 30 mm for each electrode, Figure S12) could also become realized by this proposed additive engineering. The pouched supercapacitor device with designed IL as electrolyte and AC as electrodes is shown in Figure 6a. For monolithic pouched supercapacitors, devices assembled with the designed IL have a lower R_s (0.33 Ω vs

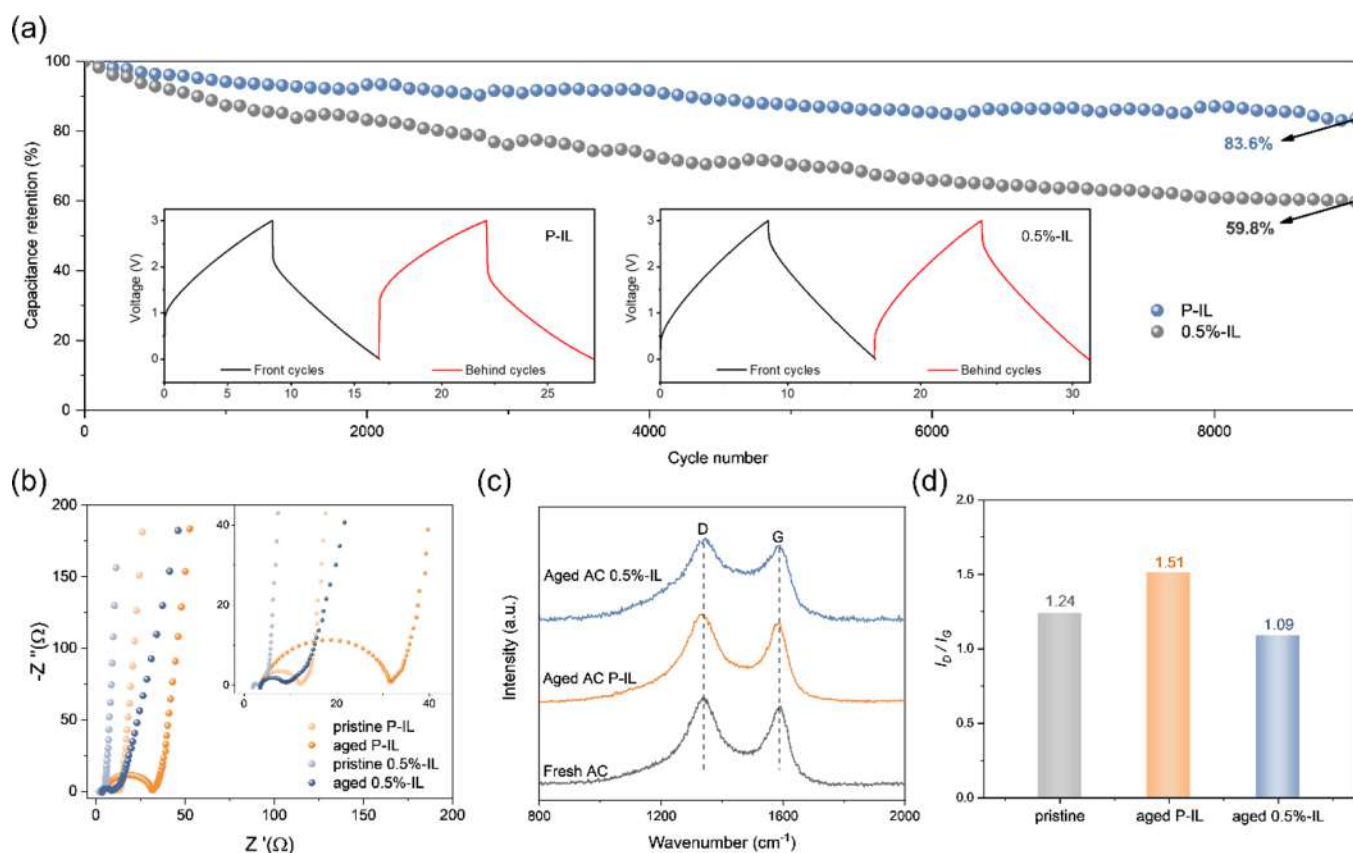


Figure 5. Cycling performance of supercapacitors. (a) Cycling stability of P-IL and 0.5%-IL supercapacitors at a current density of 5 A g^{-1} for 9000 cycles. (b) Nyquist plots of P-IL and 0.5%-IL supercapacitors before and after cycling. (c) Raman spectra of the fresh and aged AC electrodes in the different electrolytes. (d) I_D/I_G values calculated from Raman spectra.

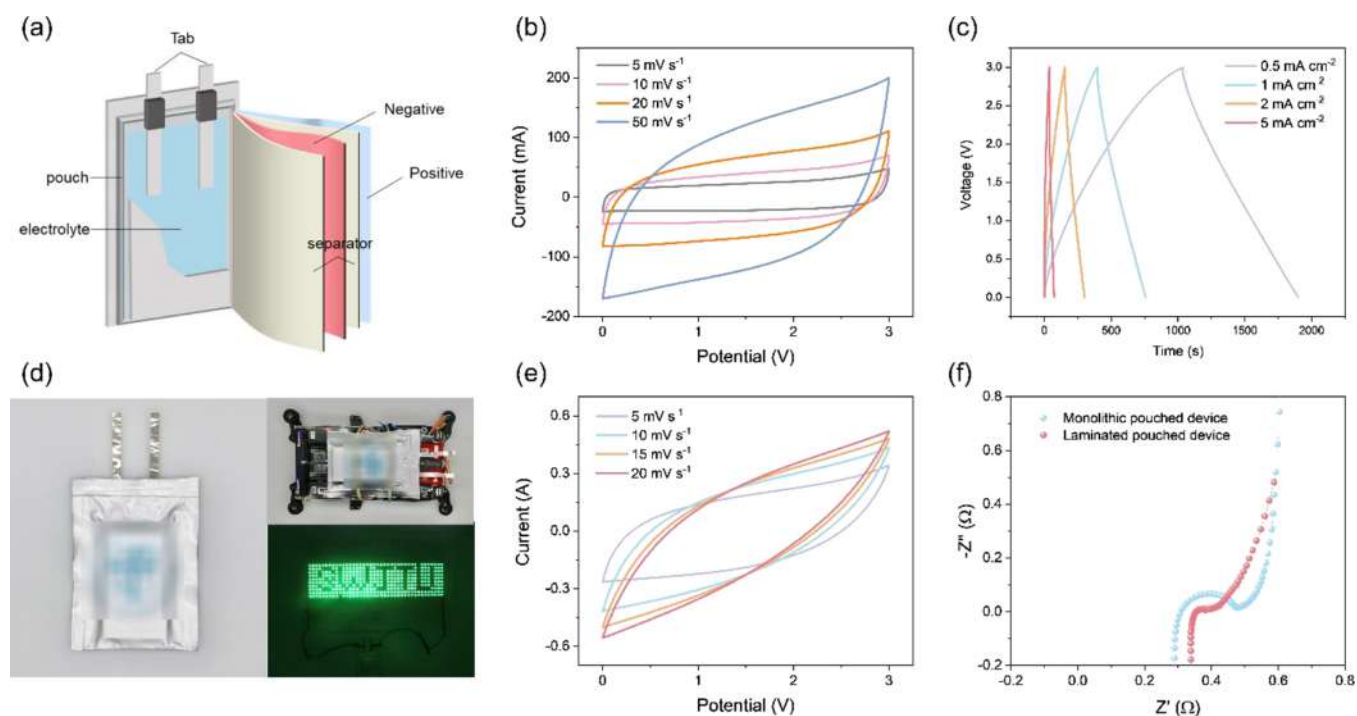


Figure 6. Practical pouches supercapacitors with additive engineering tailored EMIMBF₄ electrolytes. (a) Schematically showing the assembly of the pouches supercapacitors; (b) CV curves of the monolithic pouches device; (c) GCD curves of laminated pouches devices; (d) Toy cars could be powered by laminated pouches devices; (e) CV curves of laminated pouches devices; (f) EIS plots of monolithic and laminated pouches devices.

0.54 Ω) and higher ion diffusion coefficient (3.04×10^{-9} and $3.69 \times 10^{-9} \text{ cm}^2 \text{ s}^{-1}$) than devices with neat EMIMBF₄ (Figure S13), which indicates that the designed IL can also achieve faster ion diffusion in soft pack devices. Figure 6b shows the CV curves of the pouched devices at scan rates from 5 to 50 mV s⁻¹ in a potential window of 0–3 V, which are similar to that observed in the coin-typed cell configuration. The GCD curves of the pouched devices are exhibited in Figure 6c, and the specific capacitances calculated are 18.29, 15.54, 12.94, and 8.89 F g⁻¹ based on the GCD curves at current densities of 0.5, 1, 2, and 5 mA cm⁻², respectively. As a visualized demo, a toy car and a “SWJTU” LED bulbs can be successfully driven and/or lightened by laminated pouched devices (Figure 6d). Intriguingly, the toy car could be powered for 28 s continuously (Movie S1), indicating the potential of real application. The CV curves of pouched supercapacitors at different scan rates are similar to those of the coin-typed supercapacitors (Figure 6e). Figure 6f shows the electrochemical impedance spectroscopy (EIS) of single and stacked pouched devices; both of them have small R_{ct} demonstrating the capability of supporting high-power performance enabled by additive engineering.

CONCLUSIONS

In conclusion, we developed a new type of additive engineering by introducing additional Ti₃C₂-CTAB into typical supercapacitor electrolytes including EMIMBF₄ and Et₄NBF₄/PC. The electrostatic interaction and generated hydrogen bonds between Ti₃C₂-CTAB and electrolytes are favorable for the dissociation of electrolyte ions. Importantly, Ti₃C₂-CTAB improved the ionic conductivity without sacrificing the electrochemical stability window of the original electrolyte. Consequently, comparing supercapacitors with neat EMIMBF₄ electrolyte, the 0.5%-IL electrolyte-assembled supercapacitors showed greatly enhanced rate capability (76.4% vs 45.8%), high specific capacitance (29.6 F g⁻¹ vs 21.6 F g⁻¹), and a long cycling life (83.6% vs 59.8%). Designing better electrolytes by additive engineering opens up opportunities to solve the paradox between better ionic conductivity and the higher stable potential window of the electrolytes, which is beneficial to develop simultaneously high-power and high-energy electrochemical energy storage devices.

EXPERIMENTAL SECTION

Materials. CTAB, 1-ethyl-3-methylimidazolium tetrafluoroborate (EMIMBF₄, 98%), and 1-butyl-3-methylimidazolium tetrafluoroborate (BMIMBF₄) were purchased from Aladdin (Shanghai, China). Hydrochloric acid (36.5%, wt/wt in water) was purchased from Chengdu Kelong Chemicals Co. (Chengdu, China). Sodium carboxymethyl cellulose (C₈H₁₁O₇Na) was purchased from DAICEL Corporation (Japan), and styrene butadiene rubber (SBR) was purchased from Zeon Corporation (Japan). Conductive carbon black (Super C45) was purchased from Timical Corporation (Switzerland). Activated carbon (YP50) was purchased from Kararay (Japan). MAX phase (400 mesh) was purchased from 11 technology Co. Ltd. (Jilin, China). Cellulose separators (TF4030) were purchased from Nippon Kodoshi Corporation (Japan).

Preparation of Ti₃C₂ MXene. In a typical experiment, 2 g of LiF was dissolved in 40 mL of 9 M HCl aqueous solution and stirred for a few minutes, and 2 g of MAX phase was slowly added to the aqueous LiF/HCl solution, followed by magnetic stirring at 40 °C for 24 h. The solid residue obtained was washed several times with deionized water, centrifuged at 3500 rpm until the pH value of the supernatant became neutral, then filtered with a pore size of 0.45 μm filter

membrane, and finally dried at 40 °C for 24 h to obtain Ti₃C₂T_x (T = O, OH, F), shortened as Ti₃C₂ for convenience.

Preparation of Ti₃C₂-CTAB. First, 0.1 g of Ti₃C₂ powder and 0.1 g of cationic surfactant CTAB were added to 40 mL of deionized water and stirred magnetically at 40 °C for 24 h. Finally, the solid product was washed several times with deionized water, drying at 40 °C for 24 h to obtain Ti₃C₂-CTAB. For comparison, we also prepared EMIMBF₄ electrolytes containing 0.5 wt % of Ti₃C₂ or CTAB, which were labeled as Ti₃C₂-IL and CTAB-IL, respectively.

Preparation of Ti₃C₂-CTAB@EMIMBF₄ Electrolyte. Ti₃C₂-CTAB was mixed with EMIMBF₄ at mass ratios of 0.1:100, 0.5:100, and 1:100. Then, the mixture was sonicated for 20 min. According to the mass ratios, the obtained electrolytes were denoted as 0.1%-IL, 0.5%-IL, and 1%-IL.

Fabrication of Supercapacitors. YP50, super C45, CMC (1% aqueous solution), and SBR were mixed in a mass ratio of 85:8:2:5. After being ball milled at 300 rpm for 4 h, the slurry was coated on aluminum foil with a thickness of 20 μm . Then, the Al-supported slurry was dried at 100 °C for 12 h. The dried electrode had a thickness of $\sim 80 \mu\text{m}$, including the thickness of the Al current collector, cut into disks with a diameter of 12 mm. Finally, the CR2032 coin-type cells were assembled with two symmetrical AC electrodes of the same quality in a glove box, polypropylene diaphragm as the separator, and P-IL, 0.1%-IL, 0.5%-IL, and 1%-IL as the electrolyte. For soft-pack devices, symmetrical AC electrodes were sealed up in aluminum plastic films with a heat-sealing machine (electrode thicknesses of ~ 80 and $\sim 120 \mu\text{m}$ for monolithic and laminated pouched devices, respectively), polypropylene diaphragm as the separator, and 0.5%-IL as the electrolyte, and the weight ratio of electrolyte to electrode was set to be 2.5:1.

Material Characterization. XRD measurements were characterized on a PANalytical X'pert power diffractometer (Cu K α radiation). The ionic conductivity of the IL electrolytes was characterized using a DDB-303A conductivity meter (Rex Electric Chemical, China). The viscosity of IL electrolytes was tested by an SOC100VA fully automated viscometer. TGA was carried out with an STA449F3 thermogravimetric analyzer (NETZSCH) at a heating rate 10 °C min⁻¹ under nitrogen over temperature range 30–700 °C. The wetting ability of activated carbon electrodes with different electrolytes is tested on a contact angle analysis instrument (KRÜSS DSA100). Raman spectra were characterized by an RM2000 microscopic confocal Raman spectrometer. A TENSOR II spectrometer (Bruker) was used to confirm the type of functional group in the FTIR spectra. NMR tests were performed on a Bruker AV II-600 MHz.

Electrochemical Property Characterization. EIS, CV, and GCD measurements of coin-typed supercapacitors were performed on a CHI660E electrochemical workstation (Chenhua, Shanghai, China). The EIS, CV, and GCD measurements of soft-package supercapacitors were performed on an Admiral squidstat plus (prime 1645, America). Cyclic stability was performed on an MSTAT4 electrochemical workstation (Arbin Instruments, America). LSV measurement was performed using a conventional three-electrode system. The platinum foil was used as the working/counter electrode and Ag/AgCl as the reference electrode.

The CV curve calculates the specific capacitance (C, F g⁻¹) with the following equation:

$$C = \frac{It}{m\Delta V} \quad (2)$$

where I (A) is the discharge current, t (s) is the discharge time, m (g) is the mass of the active material, and ΔV (V) is the discharge voltage window.

The energy density (E , Wh kg⁻¹) and power density (P , kW kg⁻¹) of the assembled supercapacitor are calculated according to the following equation, respectively.

$$E = \frac{1}{2 \times 3.6} CV^2 \quad (3)$$

$$P = \frac{E}{t} \quad (4)$$

■ ASSOCIATED CONTENT

SI Supporting Information

The Supporting Information is available free of charge at <https://pubs.acs.org/doi/10.1021/acssuschemeng.3c00213>.

XRD spectra of Ti_3C_2 and Ti_3C_2 -CTAB; TGA curves of Ti_3C_2 , CTAB, and Ti_3C_2 -CTAB; optical image of Ti_3C_2 -IL; Raman full spectrum of P-IL, 0.5%-IL, Ti_3C_2 -IL, and CTAB-IL; ATR-IR full spectrum of P-IL and 0.5%-IL; TGA and DTG curves of P-IL and 0.5%-IL; LSV curves of P-IL and 0.5%-IL; CV and GCD curves of supercapacitors based on P-IL, 0.1%-IL, 0.5%-IL, and 1%-IL; electrochemical performance comparison of P-IL and 0.5%-IL supercapacitors at high and low temperatures; EIS plots of neat $\text{Et}_4\text{NBF}_4/\text{PC}$ and $\text{Et}_4\text{NBF}_4/\text{PC}@0.5 \text{ wt } \% \text{ Ti}_3\text{C}_2$ -CTAB; GCD curves of laminated pouched devices; EIS plots of P-IL and 0.5%-IL monolithic pouched devices; ionic conductivity of electrolytes; ^1H -NMR chemical shifts of P-IL and 0.5%-IL; and the performance of additive engineering-based supercapacitors in comparison with previously reported studies (PDF)

Toy car powered for 28 s continuously (MP4)

■ AUTHOR INFORMATION

Corresponding Author

Haitao Zhang – Key Laboratory of Advanced Technologies of Materials, Ministry of Education, School of Materials Science and Engineering, Southwest Jiaotong University, Chengdu 610031, China; orcid.org/0000-0002-2057-7654; Email: haitaozhang@swjtu.edu.cn

Authors

Xinglin Jiang – Key Laboratory of Advanced Technologies of Materials, Ministry of Education, School of Materials Science and Engineering, Southwest Jiaotong University, Chengdu 610031, China

Xinzheng Wu – Shanghai Suyu New Energy Co., Ltd., Shanghai 201611, P. R. China

Yanting Xie – Key Laboratory of Advanced Technologies of Materials, Ministry of Education, School of Materials Science and Engineering, Southwest Jiaotong University, Chengdu 610031, China

Zixing Wang – College of Materials Science and Engineering, Hunan Joint International Laboratory of Advanced Materials and Technology of Clean Energy, Hunan Province Key Laboratory for Advanced Carbon Materials and Applied Technology, Hunan University, Changsha 410082, P. R. China

Junfeng Huang – Key Laboratory of Advanced Technologies of Materials, Ministry of Education, School of Materials Science and Engineering, Southwest Jiaotong University, Chengdu 610031, China

Yuanxiao Qu – Key Laboratory of Advanced Technologies of Materials, Ministry of Education, School of Materials Science and Engineering, Southwest Jiaotong University, Chengdu 610031, China

Dali Mu – Key Laboratory of Advanced Technologies of Materials, Ministry of Education, School of Materials Science

and Engineering, Southwest Jiaotong University, Chengdu 610031, China

Xiong Zhang – Institute of Electrical Engineering, Chinese Academy of Sciences, Beijing 100190, P. R. China; orcid.org/0000-0001-9760-5206

Weiqing Yang – Key Laboratory of Advanced Technologies of Materials, Ministry of Education, School of Materials Science and Engineering, Southwest Jiaotong University, Chengdu 610031, China; orcid.org/0000-0001-8828-9862

Complete contact information is available at:

<https://pubs.acs.org/doi/10.1021/acssuschemeng.3c00213>

Notes

The authors declare no competing financial interest.

■ ACKNOWLEDGMENTS

The acknowledgements come at the end of an article after the conclusions and before the notes and references. This work was supported by the National Natural Science Foundation of China (Nos. 51977185 and No. 51972277) and the Sichuan Science and Technology Program (No. 23NSFSC0954). We are thankful to the Analytical and Testing Center of Southwest Jiaotong University for providing the Raman measurements.

■ REFERENCES

- (1) Liu, L.; Niu, Z.; Chen, J. Unconventional supercapacitors from nanocarbon-based electrode materials to device configurations. *Chem. Soc. Rev.* **2016**, *45*, 4340–4363.
- (2) Kumar, S.; Saeed, G.; Zhu, L.; Hui, K. N.; Kim, N. H.; Lee, J. H. 0D to 3D carbon-based networks combined with pseudocapacitive electrode material for high energy density supercapacitor: A review. *Chem. Eng. J.* **2021**, *403*, No. 126352.
- (3) Li, C.; Zhang, X.; Wang, K.; Su, F.; Chen, C.-M.; Liu, F.; Wu, Z.-S.; Ma, Y. Recent advances in carbon nanostructures prepared from carbon dioxide for high-performance supercapacitors. *J. Energy Chem.* **2021**, *54*, 352–367.
- (4) Wang, Z.; Xu, Z.; Huang, H.; Chu, X.; Xie, Y.; Xiong, D.; Yan, C.; Zhao, H.; Zhang, H.; Yang, W. Unraveling and Regulating Self-Discharge Behavior of $\text{Ti}_3\text{C}_2\text{T}_x$ MXene-Based Supercapacitors. *ACS Nano* **2020**, *14*, 4916–4924.
- (5) Chu, X.; Chen, G.; Xiao, X.; Wang, Z.; Yang, T.; Xu, Z.; Huang, H.; Wang, Y.; Yan, C.; Chen, N.; Zhang, H.; Yang, W.; Chen, J. Air-Stable Conductive Polymer Ink for Printed Wearable Micro-Supercapacitors. *Small* **2021**, *17*, No. 2100956.
- (6) Chu, X.; Wang, Y.; Cai, L.; Huang, H.; Xu, Z.; Xie, Y.; Yan, C.; Wang, Q.; Zhang, H.; Li, H.; Yang, W. Boosting the energy density of aqueous MXene-based supercapacitor by integrating 3D conducting polymer hydrogel cathode. *SusMat* **2022**, *2*, 379–390.
- (7) Pu, S.; Wang, Z.; Xie, Y.; Fan, J.; Xu, Z.; Wang, Y.; He, H.; Zhang, X.; Yang, W.; Zhang, H. Origin and Regulation of Self-Discharge in MXene Supercapacitors. *Adv. Funct. Mater.* **2023**, *33*, No. 2208715.
- (8) Chen, G.; Li, Y.; Bick, M.; Chen, J. Smart Textiles for Electricity Generation. *Chem. Rev.* **2020**, *120*, 3668–3720.
- (9) Chen, G.; Xiao, X.; Zhao, X.; Tat, T.; Bick, M.; Chen, J. Electronic Textiles for Wearable Point-of-Care Systems. *Chem. Rev.* **2022**, *122*, 3259–3291.
- (10) Libanori, A.; Chen, G.; Zhao, X.; Zhou, Y.; Chen, J. Smart textiles for personalized healthcare. *Nat. Electron.* **2022**, *5*, 142–156.
- (11) Shao, Y.; El-Kady, M. F.; Sun, J.; Li, Y.; Zhang, Q.; Zhu, M.; Wang, H.; Dunn, B.; Kaner, R. B. Design and Mechanisms of Asymmetric Supercapacitors. *Chem. Rev.* **2018**, *118*, 9233–9280.
- (12) Lv, T.; Liu, M.; Zhu, D.; Gan, L.; Chen, T. Nanocarbon-Based Materials for Flexible All-Solid-State Supercapacitors. *Adv. Mater.* **2018**, *30*, No. 1705489.

- (13) Yi, S.; Wang, L.; Zhang, X.; Li, C.; Liu, W.; Wang, K.; Sun, X.; Xu, Y.; Yang, Z.; Cao, Y.; Sun, J.; Ma, Y. Cationic intermediates assisted self-assembly two-dimensional Ti3C2Tx/rGO hybrid nano-flakes for advanced lithium-ion capacitors. *Sci. Bull.* **2021**, *66*, 914–924.
- (14) Wang, Q.; Zhou, Y.; Zhao, X.; Chen, K.; Gu, B.; Yang, T.; Zhang, H.; Yang, W.; Chen, J. Tailoring carbon nanomaterials via a molecular scissor. *Nano Today* **2021**, *36*, No. 101033.
- (15) Wang, Y.; Chu, X.; Zhu, Z.; Xiong, D.; Zhang, H.; Yang, W. Dynamically evolving 2D supramolecular polyaniline nanosheets for long-stability flexible supercapacitors. *Chem. Eng. J.* **2021**, *423*, No. 130203.
- (16) Huang, J.; Sun, T.; Ma, M.; Xu, Z.; Wang, Y.; Xie, Y.; Chu, X.; Jiang, X.; Wang, Y.; Wang, S.; Yang, W.; Zhang, H. 2D-Nb₂CT_z-supported, 3D-carbon-encapsulated, oxygen-deficient Nb₂O₅ for an advanced Li-Ion battery. *ACS Appl. Energy Mater.* **2022**, *5*, 2121–2129.
- (17) Zhang, Y.-Z.; Wang, Y.; Cheng, T.; Yao, L.-Q.; Li, X.; Lai, W.-Y.; Huang, W. Printed supercapacitors: materials, printing and applications. *Chem. Soc. Rev.* **2019**, *48*, 3229–3264.
- (18) Wang, X.; Salari, M.; Jiang, D.-E.; Chapman Varela, J.; Anasori, B.; Wesolowski, D. J.; Dai, S.; Grinstaff, M. W.; Gogotsi, Y. Electrode material-ionic liquid coupling for electrochemical energy storage. *Nat. Rev. Mater.* **2020**, *5*, 787–808.
- (19) Pal, B.; Yang, S.; Ramesh, S.; Thangadurai, V.; Jose, R. Electrolyte selection for supercapacitive devices: a critical review. *Nanoscale Adv.* **2019**, *1*, 3807–3835.
- (20) Raza, W.; Ali, F.; Raza, N.; Luo, Y.; Kim, K.-H.; Yang, J.; Kumar, S.; Mehmood, A.; Kwon, E. E. Recent advancements in supercapacitor technology. *Nano Energy* **2018**, *52*, 441–473.
- (21) Dubal, D. P.; Chodankar, N. R.; Kim, D.-H.; Gomez-Romero, P. Towards flexible solid-state supercapacitors for smart and wearable electronics. *Chem. Soc. Rev.* **2018**, *47*, 2065–2129.
- (22) Li, C.; Wu, W.; Wang, P.; Zhou, W.; Wang, J.; Chen, Y.; Fu, L.; Zhu, Y.; Wu, Y.; Huang, W. Fabricating an Aqueous Symmetric Supercapacitor with a Stable High Working Voltage of 2 V by Using an Alkaline-Acidic Electrolyte. *Adv. Sci.* **2019**, *6*, No. 1801665.
- (23) Gonzalez, A.; Goikolea, E.; Andoni Barrera, J.; Mysyk, R. Review on supercapacitors: Technologies and materials. *Renewable Sustainable Energy Rev.* **2016**, *58*, 1189–1206.
- (24) Yang, Z.; Tian, J.; Yin, Z.; Cui, C.; Qian, W.; Wei, F. Carbon nanotube- and graphene-based nanomaterials and applications in high-voltage supercapacitor: A review. *Carbon* **2019**, *141*, 467–480.
- (25) Zhong, C.; Deng, Y.; Hu, W.; Qiao, J.; Zhang, L.; Zhang, J. A review of electrolyte materials and compositions for electrochemical supercapacitors. *Chem. Soc. Rev.* **2015**, *44*, 7484–7539.
- (26) Feng, J.; Wang, Y.; Xu, Y.; Sun, Y.; Tang, Y.; Yan, X. Ion regulation of ionic liquid electrolytes for supercapacitors. *Energy Environ. Sci.* **2021**, *14*, 2859–2882.
- (27) Dhanda, M.; Arora, R.; Ahlawat, S.; Nehra, S. P.; Lata, S. Electrolyte as a panacea to contemporary scientific world of supercapacitive energy: A condense report. *J. Energy Storage* **2022**, *52*, No. 104740.
- (28) Futamura, R.; Iiyama, T.; Takasaki, Y.; Gogotsi, Y.; Biggs, M. J.; Salanne, M.; Segalini, J.; Simon, P.; Kaneko, K. Partial breaking of the Coulombic ordering of ionic liquids confined in carbon nanopores. *Nat. Mater.* **2017**, *16*, 1225.
- (29) Tsai, W.-Y.; Lin, R.; Murali, S.; Zhang, L. L.; McDonough, J. K.; Ruoff, R. S.; Taberna, P.-L.; Gogotsi, Y.; Simon, P. Outstanding performance of activated graphene based supercapacitors in ionic liquid electrolyte from -50 to 80 degrees C. *Nano Energy* **2013**, *2*, 403–411.
- (30) Cui, J.; Kobayashi, T.; Sacci, R. L.; Matsumoto, R. A.; Cummings, P. T.; Pruski, M. Diffusivity and Structure of Room Temperature Ionic Liquid in Various Organic Solvents. *J. Phys. Chem. B* **2020**, *124*, 9931–9937.
- (31) Wong, S. I.; Lin, H.; Sunarso, J.; Wong, B. T.; Jia, B. Optimization of ionic-liquid based electrolyte concentration for high-energy density graphene supercapacitors. *Appl. Mater. Today* **2020**, *18*, No. 100522.
- (32) Mourad, E.; Coustan, L.; Lannelongue, P.; Zigah, D.; Mehdi, A.; Vioux, A.; Freunberger, S. A.; Favier, F.; Fontaine, O. Biredox ionic liquids with solid-like redox density in the liquid state for high-energy supercapacitors. *Nat. Mater.* **2017**, *16*, 446.
- (33) Navalpotro, P.; Palma, J.; Anderson, M.; Marcilla, R. High performance hybrid supercapacitors by using para-Benzoquinone ionic liquid redox electrolyte. *J. Power Sources* **2016**, *306*, 711–717.
- (34) Miao, L.; Song, Z.; Zhu, D.; Li, L.; Gan, L.; Liu, M. Ionic Liquids for Supercapacitive Energy Storage: A Mini-Review. *Energy Fuels* **2021**, *35*, 8443–8455.
- (35) Wu, W.; Zhao, W.; Sun, Q.; Yu, B.; Yin, X.; Cao, X.; Feng, Y.; Li, R. K. Y.; Qu, J. Surface treatment of two dimensional MXene for poly(vinylidene fluoride) nanocomposites with tunable dielectric permittivity. *Compos. Commun.* **2021**, *23*, No. 100562.
- (36) Eftekhari, A. Supercapacitors utilising ionic liquids. *Energy Storage Mater.* **2017**, *9*, 47–69.
- (37) Berg, R. W.; Deetlefs, M.; Seddon, K. R.; Shim, I.; Thompson, J. M. Raman and ab initio studies of simple and binary 1-alkyl-3-methylimidazolium ionic liquids. *J. Phys. Chem. B* **2005**, *109*, 19018–19025.
- (38) Katsyuba, S. A.; Vener, M. V.; Zvereva, E. E.; Fei, Z.; Scopelliti, R.; Laurenczy, G.; Yan, N.; Paunescu, E.; Dyson, P. J. How Strong Is Hydrogen Bonding in Ionic Liquids? Combined X-ray Crystallographic, Infrared/Raman Spectroscopic, and Density Functional Theory Study. *J. Phys. Chem. B* **2013**, *117*, 9094–9105.
- (39) Kashyap, H. K.; Biswas, R. Solvation Dynamics of Dipolar Probes in Dipolar Room Temperature Ionic Liquids: Separation of Ion-Dipole and Dipole-Dipole Interaction Contributions. *J. Phys. Chem. B* **2010**, *114*, 254–268.
- (40) Tian, J.; Cui, C.; Xie, Q.; Qian, W.; Xue, C.; Miao, Y.; Jin, Y.; Zhang, G.; Guo, B. EMIMBF₄-GBL binary electrolyte working at 70 degrees C and 3.7 V for a high performance graphene-based capacitor. *J. Mater. Chem. A* **2018**, *6*, 3593–3601.
- (41) Forse, A. C.; Griffin, J. M.; Merlet, C.; Bayley, P. M.; Wang, H.; Simon, P.; Grey, C. P. NMR Study of Ion Dynamics and Charge Storage in Ionic Liquid Supercapacitors. *J. Am. Chem. Soc.* **2015**, *137*, 7231–7242.
- (42) Li, J.; Zhou, Y.; Tian, J.; Peng, L.; Deng, J.; Wang, N.; Qian, W.; Chu, W. A nitrogen-doped mesopore-dominated carbon electrode allied with anti-freezing EMIBF₄-GBL electrolyte for superior low-temperature supercapacitors. *J. Mater. Chem. A* **2020**, *8*, 10386–10394.
- (43) Lin, W. J.; Xu, Y.; MacDonald, S.; Gunckel, R.; Zhao, Z.; Dai, L. L. Tailoring intermolecular interactions to develop a low-temperature electrolyte system consisting of 1-butyl-3-methylimidazolium iodide and organic solvents. *RSC Adv.* **2019**, *9*, 36796–36807.
- (44) Chu, D.; Dai, P.; Luo, X.; Zhang, Y. Research progress of solid surface tension calculation based on contact angle method. *Sci. Tech. Eng.* **2021**, *7*, 3057.
- (45) Yu, J.; Yu, C.; Guo, W.; Wang, Z.; Li, S.; Chang, J.; Tan, X.; Ding, Y.; Zhang, M.; Yang, L.; Xie, Y.; Fu, R.; Qiu, J. Decoupling and correlating the ion transport by engineering 2D carbon nanosheets for enhanced charge storage. *Nano Energy* **2019**, *64*, No. 103921.
- (46) Ahuja, P.; Sharma, R. K.; Singh, G. Solid-state, high-performance supercapacitor using graphene nanoribbons embedded with zinc manganite. *J. Mater. Chem. A* **2015**, *3*, 4931–4937.
- (47) Pech, D.; Brunet, M.; Durou, H.; Huang, P.; Mochalin, V.; Gogotsi, Y.; Taberna, P.-L.; Simon, P. Ultrahigh-power micrometre-sized supercapacitors based on onion-like carbon. *Nat. Nanotechnol.* **2010**, *5*, 651–654.
- (48) Suarez, L.; Barranco, V.; Centeno, T. A. Impact of carbon pores size on ionic liquid based-supercapacitor performance. *J. Colloid Interface Sci.* **2021**, *588*, 705–712.
- (49) Tang, X.; Xiao, D.; Xu, Z.; Liu, Q.; Ding, B.; Dou, H.; Zhang, X. A novel ionic liquid-based electrolyte assisting the high performance of low-temperature supercapacitors. *J. Mater. Chem. A* **2022**, *10*, 18374–18382.

(50) Anouti, M.; Timperman, L. A pyrrolidinium nitrate protic ionic liquid-based electrolyte for very low-temperature electrical double-layer capacitors. *Phys. Chem. Chem. Phys.* **2013**, *15*, 6539–6548.

(51) Liu, W.; Yan, X.; Lang, J.; Xue, Q. Electrochemical behavior of graphene nanosheets in alkylimidazolium tetrafluoroborate ionic liquid electrolytes: influences of organic solvents and the alkyl chains. *J. Mater. Chem.* **2011**, *21*, 13205–13212.

(52) Zhang, X.; Zhao, D.; Zhao, Y.; Tang, P.; Shen, Y.; Xu, C.; Li, H.; Xiao, Y. High performance asymmetric supercapacitor based on MnO₂ electrode in ionic liquid electrolyte. *J. Mater. Chem. A* **2013**, *1*, 3706–3712.

(53) Kong, C.; Qian, W.; Zheng, C.; Yu, Y.; Cui, C.; Wei, F. Raising the performance of a 4 V supercapacitor based on an EMIBF₄-single walled carbon nanotube nanofluid electrolyte. *Chem. Commun.* **2013**, *49*, 10727–10729.

(54) Liu, W.; Yan, X.; Lang, J.; Xue, Q. Effects of concentration and temperature of EMIMBF₄/acetonitrile electrolyte on the supercapacitive behavior of graphene nanosheets. *J. Mater. Chem.* **2012**, *22*, 8853–8861.

(55) Chen, Z.; Li, Z.; Ma, X.; Wang, Y.; Zhou, Q.; Zhang, S. A new DMF-derived ionic liquid with ultra-high conductivity for high-capacitance electrolyte in electric double-layer capacitor. *Electrochim. Acta* **2019**, *319*, 843–848.

(56) Khalid, S.; Cao, C.; Naveed, M.; Younas, W. 3D hierarchical MnO₂ microspheres: a prospective material for high performance supercapacitors and lithium-ion batteries. *Sustain. Energy Fuels* **2017**, *1*, 1795–1804.

(57) Li, S.; Tian, Q.; Chen, J.; Chen, Y.; Guo, P.; Wei, C.; Cui, P.; Jiang, J.; Li, X.; Xu, Q. An intrinsically non-flammable organic electrolyte for wide temperature range supercapacitors. *Chem. Eng. J.* **2023**, *457*, No. 141265.

(58) Yang, X.; Zhang, F.; Zhang, L.; Zhang, T.; Huang, Y.; Chen, Y. A high-performance graphene oxide-doped ion gel as gel polymer electrolyte for all-solid-state supercapacitor applications. *Adv. Funct. Mater.* **2013**, *23*, 3353–3360.

(59) Le, T.; Gentile, P.; Bidan, G.; Aradilla, D. New electrolyte mixture of propylene carbonate and butyltrimethylammonium bis(trifluoromethylsulfonyl) imide (N-1114 TFSI) for high performance silicon nanowire (SiNW)-based supercapacitor applications. *Electrochim. Acta* **2017**, *254*, 368–374.

(60) Sathyamoorthi, S.; Suryanarayanan, V.; Velayutham, D. Organo-redox shuttle promoted protic ionic liquid electrolyte for supercapacitor. *J. Power Sources* **2015**, *274*, 1135–1139.

(61) Wu, J.-B.; Lin, M.-L.; Cong, X.; Liu, H.-N.; Tan, P.-H. Raman spectroscopy of graphene-based materials and its applications in related devices. *Chem. Soc. Rev.* **2018**, *47*, 1822–1873.

Recommended by ACS

Flame-Retardant Gel Electrolyte toward High-Safety Lithium Metal Batteries with High-Mass-Loading Cathodes

Geng Tang, Zhe Chen, *et al.*

MAY 15, 2023

THE JOURNAL OF PHYSICAL CHEMISTRY C

READ 

Salt-Concentrated Siloxane-Based Electrolytes for Lithium Metal Batteries: Physical Properties, Electrochemical Properties, and Cell Performance

Asuman Celik-Kucuk and Takeshi Abe

APRIL 21, 2023

ACS APPLIED ENERGY MATERIALS

READ 

Size Effect of Electrolyte Ions on the Electric Double-Layer Structure and Supercapacitive Behavior

Hoai Van Thi Nguyen, Kyung-Koo Lee, *et al.*

FEBRUARY 28, 2023

ACS APPLIED ENERGY MATERIALS

READ 

Constructing a Stabilized Cathode Electrolyte Interphase for High-Voltage LiCoO₂ Batteries via the Phenylmaleic Anhydride Additive

Xi Liu, Liyi Ye, *et al.*

JANUARY 19, 2023

ACS APPLIED ENERGY MATERIALS

READ 

Get More Suggestions >